The extended Baryon Oscillation Spectroscopic Survey: testing a new approach to measure the evolution of the structure growth

Rossana Ruggeri,[1]★ Will J. Percival,[1] Eva-Maria Mueller,[1] Héctor Gil-Marín [2,3]
Fangzhou Zhu,[4] Nikhil Padmanabhan [4] and Gong-Bo Zhao[1,5]

[1] *Institute of Cosmology and Gravitation, University of Portsmouth, Dennis Sciama Building, Portsmouth PO1 3FX, UK*
[2] *Institut Lagrange de Paris (ILP), Sorbonne Université, 98 bis Boulevard Arago, F-75014 Paris, France*
[3] *Laboratoire de Physique Nucléaire et de Hautes Energies, Université Pierre et Marie Curie, Paris, 75005, France*
[4] *Department of Physics, Yale University, New Haven, CT 06511, USA*
[5] *National Astronomy Observatories, Chinese Academy of Science, Beijing 100012, China*

ABSTRACT

The extended Baryon Oscillation Spectroscopic Survey (eBOSS) is one of the first of a new generation of galaxy redshift surveys that will cover a large range in redshift with sufficient resolution to measure the baryon acoustic oscillations signal. For surveys covering a large redshift range we can no longer ignore cosmological evolution, meaning that either the redshift shells analysed have to be significantly narrower than the survey, or we have to allow for the averaging over evolving quantities. Both of these have the potential to remove signal: analysing small volumes increases the size of the Fourier window function, reducing the large-scale information, while averaging over evolving quantities can, if not performed carefully, remove differential information. It will be important to measure cosmological evolution from these surveys to explore and discriminate between models. We apply a method to optimally extract this differential information to mock catalogues designed to mimic the eBOSS quasar sample. By applying a set of weights to extract redshift-space distortion measurements as a function of redshift, we demonstrate an analysis that does not invoke the problems discussed above. We show that our estimator gives unbiased constraints.

Key words: cosmology: observations – dark energy – large-scale structure of Universe.

1 INTRODUCTION

The extended Baryon Oscillation Spectroscopic Survey (eBOSS; Dawson et al. 2016; Zhao et al. 2016; Blanton et al. 2017), which commenced in 2014 July, will cover the largest volume to date of any cosmological redshift survey with a density sufficient to extract useful cosmological information. eBOSS observations will target multiple density-field tracers, including more than 250 000 luminous red galaxies (LRGs), 195 000 emission line galaxies (ELGs) at effective redshifts $z = 0.72$ and 0.87 and over 500 000 quasars in the range $0.8 < z < 2.2$. The survey's goals include the distance measurement at 1–2 per cent accuracy with the baryon acoustic oscillations (BAO) peak on the LRG sample and the first BAO measurements using quasars as density tracers over the redshift range $1 < z < 2$ (the first clustering measurements were recently presented in Ata et al. 2018). The wide redshift range covered compared with that in previous redshift surveys represents a unique opportunity to test and discriminate between different

cosmological scenarios on the basis of their evolution in redshift. Full survey details can be found in Dawson et al. (2016).

The clustering analysis strategy adopted for most recent galaxy survey analyses was based on computing the correlation function or the power spectrum for individual samples or subsamples, over which the parameters being measured were assumed to be unvarying with redshift. The measurements were then considered to have been made at an effective redshift (see e.g. Anderson et al. 2014; Alam et al. 2017). In particular, Alam et al. (2017) divided the full the Baryon Oscillation Spectroscopic Survey (BOSS) volume in three overlapping redshift bins and repeated the measurement in each subvolume. This technique has many disadvantages: the choice of bins is a balance between having enough data for a significant detection in each bin leading to Gaussian errors and having bins small enough that there is no cosmological evolution across them, leading to a degrading compromise. The technique also ignores information from the cross-correlation between galaxies in different redshift bins, potentially ignoring signal. Sharp cuts in redshift will also introduce ringing artefacts in the Fourier space, potentially causing complications in the analysis.

★ E-mail: rossana.ruggeri@port.ac.uk

To complicate analyses further, many mock catalogues currently used to compare to the data intrinsically lack evolution, or 'light-cone' effects, being drawn from simulation snapshots. Although this is a separate problem, these differences limit the tests of the effects of evolution that can be performed, and have the potential to hide biases caused by evolution.

Recent work by Zhu, Padmanabhan & White (2015), Ruggeri et al. (2017), and Mueller, Percival & Ruggeri (2018) introduced an alternative approach to the redshift binning. The idea is to consider the whole volume of the survey and optimally compress the information in the redshift direction by applying a set of redshift weights to all galaxies, and only then computing the weighted correlation function. Comparing measurements made using different sets of redshift weights maintains the sensitivity to the underlying evolving theory. The sets of weights are derived in order to minimize the error on the parameters of interest. In addition, by applying the redshift weighting technique instead of splitting the survey, is it possible to compute the correlation function to larger scales whilst accounting for the evolution in redshift; this was particularly clear in Mueller et al. (2018), which considered this method to optimize the measurement of local primordial non-Gaussianity, which relies on large scales. Further, Zhu et al. (2016) showed that the application of a weighting scheme rather than splitting into bins also improves BAO measurements.

The need to correctly deal with evolution will increase for the Dark Energy Spectroscopic Instrument (DESI) and *Euclid* experiments, which will cover a broad redshift range and have significantly reduced statistical measurement errors compared to current surveys in any particular redshift range. The DESI[1] is a new multi-object spectrograph (MOS) currently under construction for the 4-m Mayall Telescope on Kitt Peak. DESI will be able to obtain 5000 simultaneous spectra, which coupled with the increased collecting area of the telescope compared with the 2.5-m Sloan telescope, means that it can create a spectroscopic survey of galaxies ∼20 times more quickly than eBOSS. In 2020 the European Space Agency (ESA) will launch the *Euclid*[2] satellite mission. *Euclid* is an ESA medium class astronomy and astrophysics space mission, and will undertake a galaxy redshift survey over the redshift range $0.9 < z < 1.8$, while simultaneously performing an imaging survey in both visible and near-infrared bands. The complete survey will provide hundreds of thousands images and several tens of petabytes of data. About 10 billion sources will be observed by *Euclid* out of which several tens of million galaxy redshifts will be measured and used to make galaxy clustering measurements.

In this work, we test the redshift weighting approach by analysing a set of 1000 mocks catalogues (Chuang et al. 2015) designed to match the eBOSS quasar sample. This quasar sample has a low density (82.6 objects deg^{-2}) compared to that of recent galaxy samples, and covers a total area over 7500 deg^2. The quasars are highly biased targets and we expect their bias to evolve with redshift, $b(z) \propto c_1 + c_2(1 + z)^2$, with constant values $c_1 = 0.607 \pm 0.257$, $c_2 = 0.274 \pm 0.035$, as measured in Laurent et al. (2017).

Although the mocks are not drawn from *N*-body simulations, they have been calibrated to match one of the BigMultiDark (BigMD; Klypin et al. 2016), a high-resolution *N*-body simulation, with 3840^3 particles covering a volume of $(2500 \, h^{-1} \, Mpc)^3$. The BigMD simulations were performed using GADGET-2 (Springel 2005), with

Λ cold dark matter (ΛCDM) *Planck* cosmological constraints as a fiducial cosmology. $\Omega_m = 0.307$, $\Omega_b = 0.048206$, $\sigma_8 = 0.8288$, $n_s = 0.96$, $H_0 = 100 \, h \, km \, s^{-1} \, Mpc^{-1}$, and $h = 0.6777$. In Chuang et al. (2015) the authors showed that effective Zel'dovich approximation mocks (EZmocks) are nearly indistinguishable from the full *N*-body solutions: they reproduce the power spectrum within 1 per cent, up to $k = 0.65 \, h \, Mpc^{-1}$. The mocks are created using a new efficient methodology based on the effective Zel'dovich approximation approach including stochastic scale-dependent, non-local, and non-linear biasing contribution. The EZmocks used for the current analysis are the light-cone catalogues, realized on seven different snapshots at $z = 0.9, 1.1, 1.3, 1.5, 1.6, 1.7$, and 2.0. The full simulations incorporate the redshift evolution for f, σ_8, the BAO damping, and the non-linear density and velocity effects.

In a companion paper (Ruggeri et al. 2017), we will apply the weighting scheme to measure redshift-space distortions (RSDs) from the eBOSS Data Release 14 (DR14) quasar data. In this paper, we validate the procedure and test for optimality. By fitting to the evolution with a model for bias and cosmology, we are able to fit simultaneously the evolution of the growth rate $f(z)$, the amplitude of the dark matter density fluctuations $\sigma_8(z)$, and the galaxy bias $b(z)$; breaking part of the degeneracy inherent in standard measurements of $f\sigma_8$ and $b\sigma_8$ when only one effective redshift is considered. We show that the redshift weighting scheme gives unbiased measurements.

The weights can be applied in both configuration and Fourier space. In this paper, we focus on Fourier space, as there is some evidence that this provides stronger RSDs constrains, given the current scale limits within which the clustering can be modelled to a reasonable accuracy (Alam et al. 2017). In addition, the calculation of the power spectrum moments is significantly faster than the correlation function (Bianchi et al. 2015; Scoccimarro 2015). Working in Fourier space requires a reformulation of the window selection to account for an evolving power spectrum.

The paper is organized as follows. Section 2 reviews the derivation of optimal weights, presenting two schemes that differ in the cosmological model to be tested. In Section 3, we review the redshift-space power spectrum model at a single redshift; In Section 4, we model the power spectrum and the window function to obtain the redshift evolving power spectrum. In Section 5, we present the result of our analysis.

2 OPTIMAL WEIGHTS

We make use of two different sets of weights. The first explores deviations from the ΛCDM model by altering the evolution of Ω_m in redshift. This model ties together growth and geometry, but can also be used after fixing the expansion rate to match the prediction of the ΛCDM model. The second parametrizes the $f\sigma_8$ parameter combination measured by RSD, allowing for a more standard test of deviations from ΛCDM. Here, the growth and geometry are artificially kept separate as $f\sigma_8$ only affects cosmological growth. In both cases the weights are computed selecting a flat ΛCDM scenario as fiducial model. Note that, as discussed in Ruggeri et al. (2017) and Zhu et al. (2015), the choice of an inaccurate fiducial model for the weights would only affect the variance of the quantities constrained and not the best-fitting values.

The weight functions act as a smooth window on the data and allow us to combine the information coming from the whole volume sampled. These weights are derived by minimizing the error on the RSD measurements, as predicted by a simple Fisher matrix analysis

[1]http://desi.lbl.gov/
[2]http://sci.esa.int/euclid

(Ruggeri et al. 2017). Their derivation allows for the evolution with redshift of the cosmological parameters we want to estimate from the data. Optimizing the measurements of the generic parameter θ from the power spectrum moments P_j, $j = 0, 2, 4\ldots$, we obtain the following weights:

$$w(z) = \mathbf{C}^{-1} \partial P_j(z)/\partial \theta. \qquad (1)$$

We assume the covariance matrix of P, $\mathbf{C}$ to be parameter independent and, in absence of a survey window, to be described as

$$\mathbf{C} \sim (P + 1/\overline{n})^2 1/\mathrm{d}V \qquad (2)$$

for each volume element, $\mathrm{d}V$, within the survey. The weights can be seen as an extension of the Feldman–Kaiser–Peacock (FKP) weights presented in Feldman, Kaiser & Peacock (1994), which have the form

$$w_{\mathrm{FKP}}(r) = \frac{1}{1 + \overline{n}(r)P(k)} \qquad (3)$$

by including the redshift component $\partial P_j(z)/\partial \theta$.

Note that the weights as they are reported in equation (1) aim to compress different *measurements* of the power spectrum across a range of different redshifts. In fact, we apply weights to each galaxy in order to avoid binning, by assuming the relation $w_{\mathrm{gal}} = \sqrt{w_P}$, with w_P denoting the weights defined in equation (1), which relies on the scale dependence of the weights being smooth on the scale of interests for clustering.

2.1 Optimal weights for Ω_{m}

As described in Ruggeri et al. (2017), it is empirically convenient to test for deviations from the ΛCDM model by considering the evolution of the matter density with redshift. To do this, we consider a Taylor expansion up to second order about the fiducial model:

$$\frac{\Omega_{\mathrm{m}}(z)}{\Omega_{\mathrm{m,fid}}(z)} = q_0 \left[1 + q_1 y(z) + \frac{1}{2} q_2 y(z)^2 \right], \qquad (4)$$

where z_{p} is the pivot redshift, i.e. a selected redshift within the redshift range of the survey and $y(z) + 1 \equiv \Omega_{\mathrm{m,fid}}(z)/\Omega_{\mathrm{m,fid}}(z_{\mathrm{p}})$. Note that as shown in Zhu et al. (2016), the analysis does not depend on the choice of a particular z_{p}. The q_i parameters correspond to the first and second derivatives of $\Omega_{\mathrm{m}}(z)|_{z_{\mathrm{p}}}$, evaluated at z_{p}, and incorporate potential deviations about the fiducial model $\Omega_{\mathrm{m,fid}}$.

The choice of parametrizing Ω_{m} (and hence the Hubble parameter, the angular diameter distance, and the growth rate) in terms of q_0, q_1, and q_2 allows us to simultaneously investigate small deviations using a common framework: e.g. departures from a fiducial cosmology and geometry are accounted through the fiducial Hubble constant and angular diameter distance $H(\Omega_{\mathrm{m}})$, $D_{\mathrm{A}}(\Omega_{\mathrm{m}})$; further, modified gravity models can be accounted through the growth rate, $f(\Omega_{\mathrm{m}})$.

By matching to the standard Friedman equation, we parametrize the redshift evolution of the Hubble parameter in term of $\Omega_{\mathrm{m}}(z)$ as

$$H^2(z) = H_0^2 \frac{\Omega_{\mathrm{m,0}}(1 + z)^3}{\Omega_{\mathrm{m}}(z)}. \qquad (5)$$

Assuming a flat Universe ($\Omega_k = 0$) in agreement with cosmic microwave background (CMB) measurements (Planck Collaboration XIII 2016), we have $\Omega_{\Lambda}(z) = 1 - \Omega_{\mathrm{m}}(z)$. The subscript '0' denotes quantities evaluated at $z = 0$. For simplicity of notation we omit the q_i dependence from all the parameters: we refer to $\Omega_{\mathrm{m}}(z, q_i)$ as $\Omega_{\mathrm{m}}(z)$, and we denote with $\Omega_{\mathrm{m,fid}}$ the fiducial ΛCDM matter density.
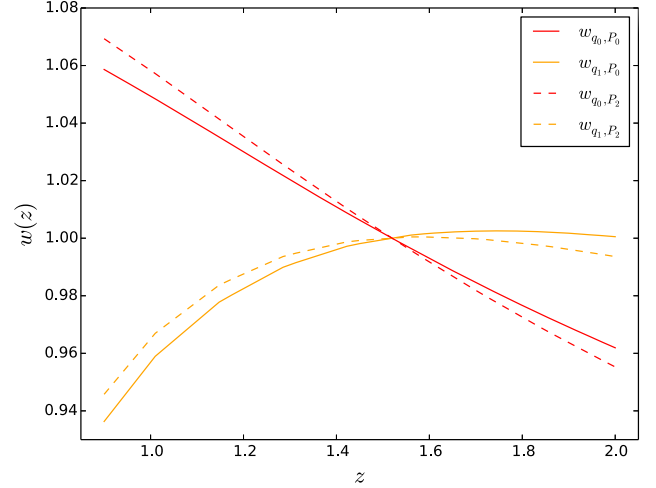
Figure 1. The weights for the monopole and quadrupole with respect to the q_i parameters.

For the scenarios considered, we assume the solution for the linear growth factor $D(z)$ and the dimensionless linear growth rate f have the same dependence on $\Omega_{\mathrm{m}}(z)$ as in the ΛCDM model:

$$g(z) \equiv (1 + z)D(z) = \frac{5\Omega_{\mathrm{m}}(z)H^3(z)}{2(1 + z)^2} \int_z^{\infty} \mathrm{d}z' \frac{(1 + z')}{H^3(z')}, \qquad (6)$$

$$f(z) = -1 - \frac{\Omega_{\mathrm{m}}(z)}{2} + \Omega_{\Lambda}(z) + \frac{5\Omega_{\mathrm{m}}(z)}{2g(z)}. \qquad (7)$$

Fig. 1 shows an example of the weights as derived in Ruggeri et al. (2017) that optimize the measurements of the q_i parameters in a ΛCDM fiducial background for a redshift-space power spectrum. Since each multipole contains information about $\Omega_{\mathrm{m}}(z)$, our set of weights is derived to be optimal for the first two non-null moments of the power spectrum on the Legendre polynomial basis for each q_i parameter. Continuous lines indicate the weights for the monopole with respect to q_0 (red line) and q_1 (orange line); dashed lines indicate the weights for the quadrupole with respect q_0, q_1 (red and orange lines). All the weights are normalized to be equal 1 at the pivot redshift.

2.2 Optimal weights for $f\sigma_8$

RSD measurements constrain the amplitude of the velocity power spectrum, and its cosmological dependence in the linear regime is commonly parametrized by the product of the two parameters f and σ_8, which provides a good discriminator of modified gravity models (Song & Percival 2009). We compare results obtained from the Ω_{m} parametrization with those derived using a set of weights parametrized with respect to $[f\sigma_8](z)$. In an analogous way to the consideration in Section 2.1, we can expand $[f\sigma_8](z)$ about a fiducial model, so equation (4) becomes

$$[f\sigma_8](z) = [f\sigma_8]_{\mathrm{fid}}(z)p_0 \left(1 + p_1 x + p_2 \frac{x^2}{2} \right), \qquad (8)$$

where $x \equiv [f\sigma_8]_{\mathrm{fid}}(z)/[f\sigma_8]_{\mathrm{fid}}(z_{\mathrm{p}}) - 1$. The p_i parameters correspond to the first and second derivatives of $[f\sigma_8](z)|_{z_{\mathrm{p}}}$, evaluated at z_{p}, and incorporate potential deviations about the fiducial model $[f\sigma_8]_{\mathrm{fid}}$.

As a fiducial model for $[f\sigma_8]_{\mathrm{fid}}$ to compute the weights, we select the solution of linear perturbation theory in a flat ΛCDM scenario,

where the growth rate evolves with redshift as

$$[f\sigma_8]_{\text{fid}}(z) = \left[-1 - \frac{\Omega_{\text{m,fid}}(z)}{2} + \Omega_{\Lambda,\text{fid}}(z) + \frac{5\Omega_{\text{m,fid}}(z)}{2g_{\text{fid}}(z)}\right]$$
$$\times \sigma_{8,0}\frac{g_{\text{fid}}(z)}{(1+z)^2}, \quad (9)$$

with g_{fid}, fiducial growth factor,

$$g_{\text{fid}}(z) = \frac{5\Omega_{\text{m,fid}}(z)H_{\text{fid}}^3(z)}{2(1+z)^2}\int_z^\infty \text{d}z' \frac{(1+z')}{H_{\text{fid}}^3(z')}. \quad (10)$$

The galaxy bias parameter is assumed to be independent of f and σ_8. For simplicity, we consider $[b\sigma_8]$ to be *independent* from $[f\sigma_8]$ as well. Considering e.g. the galaxy monopole with respect to the linear matter power spectrum P,

$$P_0 = \left([b\sigma_8]^2 + \frac{2}{3}[b\sigma_8][f\sigma_8](z) + \frac{1}{5}[f\sigma_8]^2(z)\right)P(k), \quad (11)$$

the dependence on the p_i parameters is given only through $[f\sigma_8]$. We derive the set of weights by taking the derivative of P_0, P_2, and P_4 with respect to p_1, p_2, and p_3. For completeness we include the weights here as they were not included in Ruggeri et al. (2017):

$$w_{i,p_0} = \mathbf{C}^{-1}N_i, \quad w_{i,p_1} = \mathbf{C}^{-1}N_i y, \quad w_{i,p_2} = \mathbf{C}^{-1}N_i\frac{1}{2}y^2, \quad (12)$$

where

$$N_0 \equiv \left(\frac{2}{3}[b\sigma_8] + \frac{2}{5}[f\sigma_8](z)\right)[f\sigma_8](z), \quad (13)$$

$$N_2 \equiv \left(\frac{4}{3}[b\sigma_8] + \frac{8}{7}[f\sigma_8](z)\right)[f\sigma_8](z), \quad (14)$$

$$N_2 \equiv \left(\frac{16}{35}[f\sigma_8](z)\right)[f\sigma_8](z). \quad (15)$$

A strong effect on the set of weights is caused by the assumptions we make for galaxy bias. If we set the bias as an unknown parameter, and we marginalize over it, then we cannot deduce any information about structure growth from the amplitude of the density power spectrum. Marginalizing over the bias will not affect the other parameters provided that the bias model is correct. We do not have a sufficiently accurate model of galaxy formation and evolution that the bias can be accurately predicted. As explained in Section 4.3, in this work, we describe it using free functions and making sure there is enough freedom in other parameters.

This is the case for the expansion around $[f\sigma_8]$, where we considered $[b\sigma_8]$ and $[f\sigma_8]$ as independent parameters. However, if we constrain $b(z)$ to match a fiducial model, we will derive weights that make use of the information coming from the amplitude of the power spectrum. For the expansion around Ω_{m}, we can choose whether or not to include this information.

3 MODELLING THE ANISOTROPIC GALAXY POWER SPECTRUM AT A SINGLE REDSHIFT

We model the power spectrum using perturbation theory (PT) up to one-loop order. We include the non-linear RSDs effects as in Scoccimarro (2004) and Taruya, Nishimichi & Saito (2010) (TSN model),

$$P_g(k,\mu) = \exp\left\{-(fk\mu\sigma_v)^2\right\}\left[P_{g,\delta\delta}(k)\right.$$
$$+ 2f\mu^2 P_{g,\delta\theta}(k) + f^2\mu^4 P_{\theta\theta}(k)$$
$$+ b^3 A(k,\mu,\beta) + b^4 B(k,\mu,\beta)\Big], \quad (16)$$

where μ is the cosine of the angle between the wave vector $\boldsymbol{k}$ and the line of sight (LOS). $P_{\theta\theta}$ and $P_{\delta\theta}$ are the *velocity–velocity* and *matter–velocity* power spectra terms that correspond to the extended linear model of Kaiser (1987) as derived in Scoccimarro (2004). θ denotes the Fourier transform (FT) of the comoving velocity field divergence, $\theta(\boldsymbol{k}) \equiv -i\boldsymbol{k}\cdot\boldsymbol{u}(k)$, where $\nabla\boldsymbol{u} = -\nabla\boldsymbol{v}/[af(a)H(a)]$ with velocity field v and dimensionless linear growth rate f. The exponential term represents the damping due to the 'fingers of God' effect, where σ_v denotes the velocity dispersion term, here treated as free parameter. The A, B terms come from the TNS model that take into account further corrections due to the non-linear coupling between the density and velocity fields (Taruya et al. 2010). Note that at linear level $P_{\theta\theta} = P_{\delta\theta} = P_{\delta\delta}$.

We model $P_{g,\delta\delta}$ and $P_{g,\delta\theta}$ as

$$P_{g,\delta\delta}(k) = b^2 P_{\delta\delta}(k) + 2b_2 b P_{b2,\delta}(k) + 2b_{s2}b P_{bs2,\delta}(k)$$
$$+ 2b_{3\text{nl}}b\sigma_3^2(k)P(k) + b_2^2 P_{b22}(k)$$
$$+ 2b_2 b_{s2}P_{b2s2}(k) + b_{s2}^2 P_{bs22}(k) + S, \quad (17)$$

$$P_{g,\delta\theta}(k) = b P_{\delta\theta}(k) + b_2 P_{b2,\theta}(k) + b_{s2}P_{bs2,\theta}(k)$$
$$+ b_{3\text{nl}}\sigma_3^2(k)P(k). \quad (18)$$

The bias is modelled following recent studies Chan, Scoccimarro & Sheth (2012) and Baldauf et al. (2012) that showed the importance of non-local contributions. We account for those effects introducing as galaxy bias parameters: the linear b, second-order local b_2, non-local b_{s2}, and the third-order non-local $b_{3\text{nl}}$ bias parameters, and the constant stochasticity shot noise term S. We numerically evaluate the non-linear matter power spectra, $P_{\delta\delta}$, $P_{\delta\theta}$, $P_{\theta\theta}$, at one-loop order in standard perturbation theory (SPT) using the linear power spectrum input from CAMB (Lewis & Bridle 2002).

In this analysis, we make use of the first three non-zero moments of the power spectrum, projected into an orthonormal basis of Legendre polynomials $\mathcal{L}_\ell(\mu)$ such that

$$P_\ell(k) = \frac{2\ell+1}{2}\int_{-1}^1 \text{d}\mu P(k,\mu)\mathcal{L}_\ell(\mu), \quad (19)$$

with the monopole $\ell = 0$, quadrupole $\ell = 2$, and hexadecapole $\ell = 4$, respectively. In this paper, we do not consider geometrical deviations and we are only concerned with growth measurements in a fixed background. However, we note that such deviations can be included as follows. The geometrical deviations from the fiducial cosmology can be included through the Alcock–Paczynski (AP) effect (Alcock & Paczynski 1979). Here, revised mode numbers k', μ' for the cosmological model being tested are related to those observed k, μ assuming the fiducial cosmology by the transformations:

$$k' = \frac{k}{\alpha_\perp}\left[1 + \mu^2\left(\frac{\alpha_\perp^2}{\alpha_\parallel^2} - 1\right)\right]^{1/2},$$
$$\mu' = \frac{\mu\alpha_\perp}{\alpha_\parallel}\left[1 + \mu^2\left(\frac{\alpha_\perp^2}{\alpha_\parallel^2} - 1\right)\right]^{-1/2}, \quad (20)$$

where the scaling factors $\alpha_\parallel$ and $\alpha_\perp$ are defined as

$$\alpha_\parallel = \frac{H^{\text{fid}}(z)}{H(z)},$$
$$\alpha_\perp = \frac{D_A(z)}{D_A^{\text{fid}}(z)}. \quad (21)$$

By applying the transformations of equation (21) to equation (19), the multipoles at the observed k and μ relate to the power spectrum

at the true variables k' and μ' through

$$P_\ell(k) = \frac{(2\ell+1)}{2\alpha_\perp^2 \alpha_\parallel} \int_{-1}^{1} d\mu \, P_g(k', \mu') \mathcal{L}_\ell(\mu). \tag{22}$$

4 MODELLING THE EVOLVING GALAXY POWER SPECTRUM

4.1 Redshift weighted multipoles without window function

We model the redshift dependence of f, σ_8, $\alpha_\parallel$, and $\alpha_\perp$ as described above, and the bias evolution (see Section 4.3). In principle we can compute the weighted multipoles by integrating the power spectrum moments as given in equation (22) over redshift, including the redshift weighting,

$$P_{\ell w_{\ell,q_j}} = \int dz \, P_\ell(k, z) w_{\ell,q_j}. \tag{23}$$

In general when estimating the power spectrum of a three-dimensional redshift survey that measured is the underlying power spectrum convolved with the window function. Therefore to compare the model with the data we first convolve it with the window determined by the survey geometry. In the next section, we derive a general relation between the measured P and the window function to extend the treatment of Feldman et al. (1994), (equation 2.1.4) to the case where the power spectrum is evolving with redshift.

4.2 Redshift weighted multipoles including the survey window effect

We study the window function for the evolving power spectrum using a generalized Hankel transformation between power spectrum and correlation function moments, where the window applied is also decomposed into a set of multipoles. This is an extension of the work by Wilson et al. (2017) and Beutler et al. (2017), which presented a method to convolve model power spectra with the window function for a non-evolving power spectrum. We consider the case where the underlying correlation function ξ is dependent on both the separation $r = |r_i - r_j|$ (with r_i and r_j position of galaxies of each pair) and the mean redshift of each galaxy pair $\xi[r_i(z_i), |r_i - r_j|]$. Here we have assumed that cosmological evolution is negligible over the range of redshifts covered by every pair, so we can quantify the clustering of each using the correlation function at the mean redshift.

The multipole moments of the power spectrum in the local plane-parallel approximation can be written as

$$\begin{aligned}
P_\ell(k) = & \frac{2\ell+1}{2} \int d\mu_k \int \frac{d\phi}{2\pi} \int dx_1 \int dx_2 \, e^{ik\cdot x_1} e^{-ik\cdot x_2} \\
& \times \langle \delta(x_1)\delta(x_2) W(x_1)W(x_2)\rangle \, \mathcal{L}_\ell(\hat{k}\cdot\hat{x}_h) \\
= & \frac{2\ell+1}{2} \int d\mu_k \int \frac{d\phi}{2\pi} \int dx_1 \int ds \\
& \times \left(\sum_L \xi_L[s, z(x_1)]\mathcal{L}_L(\hat{x}_h\cdot\hat{s}) \right) \\
& \times W(x_1)W(x_1+s) \, e^{-ik\cdot s}\mathcal{L}_\ell(\hat{k}\cdot\hat{x}_h),
\end{aligned} \tag{24}$$

where $\int d\mu_k$ is the integral over all the possible cosine angles between $\hat{k}$ and $\hat{x}_h$ and W defines the mask. ξ_L denotes the correlation function moments in the Legendre basis. Note that equation (24) differs from equation (A.16) in Beutler et al. (2017), only in the $\xi_L[s, z(x_1)]$ term; for a single redshift slice we would only have

$\xi_L(s)$. We make use of the relations

$$e^{-ik\cdot s} = \sum_p (i)^p (2p+1) j_p(ks)\mathcal{L}_p(\hat{k}\cdot\hat{s}), \tag{25}$$

$$\int d\mu_k \int \frac{d\phi}{2\pi} \mathcal{L}_\ell(\hat{k}\cdot\hat{x}_h)\mathcal{L}_p(\hat{k}\cdot\hat{s}) = \frac{2}{2\ell+1}\mathcal{L}_\ell(\hat{s}\cdot\hat{x}_h)\delta_{\ell p}, \tag{26}$$

which, when combined with equation (24), give

$$\begin{aligned}
P_\ell(k) = & \, i^\ell(2\ell+1) \int dx_1 \int ds \, \sum_L \xi_L[s, z(x_1)]j_\ell(ks) \\
& \times W(x_1)W(x_1+s)\mathcal{L}_\ell(\hat{x}_h\cdot\hat{s})\mathcal{L}_L(\hat{x}_h\cdot\hat{s}).
\end{aligned} \tag{27}$$

Substituting the Bailey relation, $\mathcal{L}_\ell\mathcal{L}_p = \sum_t a_{pt}^\ell \mathcal{L}_t$, equation (27) becomes

$$\begin{aligned}
P_\ell(k) = & \, i^\ell(2\ell+1) \int dx_1 \int ds \, \sum_L \xi_L[s, z(x_1)]j_\ell(ks) \\
& \times W(x_1)W(x_1+s)\mathcal{L}_\ell(\hat{x}_h\cdot\hat{s})\sum_t a_{Lt}^\ell \mathcal{L}_t(\hat{x}_h\cdot\hat{s}) \\
= & \, i^\ell(2\ell+1) \int 2\pi s^2 ds \, j_\ell(ks) \sum_L \sum_t a_{Lt}^\ell \int d\mu_s \int \frac{d\phi}{2\pi} \\
& \times \int dx_1 \, \xi_L[s, z(x_1)]W(x_1)W(x_1+s)\mathcal{L}_t(\hat{x}_h\cdot\hat{s}).
\end{aligned} \tag{28}$$

At this stage, in contrast to equation (A.19) in Beutler et al. (2017), we cannot bring ξ_L out of the integral over x_1. Since we are not able to decouple the mask from ξ, in principle, we would have to compute the integral over x_1 for every model ξ fitted to the data. However, we can reduce drastically the computational time required by assuming that ξ is well behaved such that we can split the integral over x_1 into a sum over a small number of x_i ranges. This is different from measuring the clustering in shells – we are still calculating and modelling the power spectrum as a continuously weighted function calculated using every galaxy pair; we are simply making an assumption about the smooth behaviour in redshift of the expected clustering:

$$\begin{aligned}
P_\ell(k) = & \, i^\ell(2\ell+1) \int 2\pi s^2 ds \, j_\ell(ks) \sum_L \sum_t a_{Lt}^\ell \int d\mu_s \int \frac{d\phi}{2\pi} \\
& \times \sum_i \int_{x_i} dx_1 \, \xi_L(s, z(x_i))W(x_i)W(x_i+s)\mathcal{L}_t(\hat{x}_h\cdot\hat{s}).
\end{aligned} \tag{29}$$

Assuming that $\xi_L(s, z(x_i))$ is constant over each subintegral range x_i we can take it out of the integrals,

$$\begin{aligned}
P_\ell(k) = & \, i^\ell(2\ell+1) \int 2\pi s^2 ds \, j_\ell(ks) \sum_L \sum_t a_{Lt}^\ell \\
& \times \sum_i \xi_L(s, z(x_i)) \int d\mu_s \int \frac{d\phi}{2\pi} \int_{x_i} dx_i \, W(x_i)W(x_i+s)\mathcal{L}_t(\hat{x}_h\cdot\hat{s}),
\end{aligned} \tag{30}$$

and redefine the subwindow function multipoles $W_{p,z_i}^2(s)$ for $p = 0$, 2, 4... as

$$\begin{aligned}
W_{p,z_i}^2(s) = & \frac{2p+1}{2} \int d\mu_s \int \frac{d\phi}{2\pi} \int_{z_i} dx_i \\
& \times W(x_i)W(x_i+s)\mathcal{L}_p(\mu_s).
\end{aligned} \tag{31}$$

Using the definition of the subwindow function multipoles of equation (31), we can write equation (30) to be

$$\begin{aligned}
P_\ell(k) = & \, i^\ell(2\ell+1) \int 2\pi s^2 ds \, j_\ell(ks) \\
& \times \sum_L \sum_t \frac{2}{2t+1} a_{Lt}^\ell \sum_i \xi_L(s, z_i)W_{t,z_i}^2(s),
\end{aligned} \tag{32}$$

which generalizes equation (A.23) in Beutler et al. (2017) to the case of a redshift-evolving power spectrum.

Note that when computing the mask $W(\boldsymbol{x})$ using the random catalogue we include the redshift weights, in the same way the standard FKP weights have been included in traditional analyses (e.g. Beutler et al. 2017).

4.3 Bias evolution

The evolution in redshift of the galaxy bias, $b(z)$, strongly depends on the targets considered. In Ruggeri et al. (2017) we compared the weights for different $b(z)$ relations and showed that the weights are not significantly sensitive to the different $b(z)$ considered.

The fitting formula for the linear bias parameter of the quasar sample suggests that the linear bias redshift evolves as (Laurent et al. 2017)

$$b(z) = 0.53 + 0.29(1 + z)^2. \tag{33}$$

We model the evolution of b about the pivot redshift times σ_8 as

$$b\sigma_8(z) = b\sigma_8(z_p) + \partial b\sigma_8/\partial z|_{z_p}(z - z_p) + \cdots. \tag{34}$$

We neglect the redshift dependence for the non-linear bias parameter b_2, so we assume this is constant with redshift, $b_2\sigma_8(z_{piv})$. We fix the second-order non-local bias, bs_2, and third-order non-local bias, b_{3nl}, terms to their predicted values according to non-local Lagrangian models (Baldauf et al. 2012; Chan et al. 2012):

$$b_{s2} = -\frac{4}{7}(b - 1),$$
$$b_{3nl} = \frac{32}{315}(b - 1). \tag{35}$$

5 FITTING TO THE MOCK DATA

5.1 Power spectrum measurement

To compute the power spectrum moments with respect to the LOS, we make use of the estimator introduced in Bianchi et al. (2015). This FT-based algorithm uses multiple FTs to track the multipole moments, in the local plane-parallel approximation where we have a single LOS for each pair of galaxies. This estimator has been already used in recent analysis (Beutler et al. 2017) that confirmed the advantages of using such decomposition: it reduces the computational time from N^2 associated to naive pair counting analysis (Yamamoto et al. 2006) to $\sim N\log N$.

Redshift weights are included in the estimator, by defining the weighted galaxy number density as $n_g(\boldsymbol{r})w$. As discussed in Section 2, we have derived the galaxy weights from the square-root of the power spectrum weights, under the assumption that the scale dependence in the weights is smooth compared to the scale of interest for our clustering measurements.

The result is a set of weighted multipoles, $P_{0,2,w_{0,1,2}}$, where each P_{i,w_j} corresponds to a particular set of weights that optimizes each of the q_i or p_i measurement, i.e. for the set of weights w_{i,q_j} (or w_{i,p_j} for the $f\sigma_8$ weights) functions, and we build a data vector Π as

$$\Pi = (P_{0,w_0,q_0}, P_{0,w_0,q_1}, P_{0,w_0,q_2}, \ldots P_{2,w_2,q_2}). \tag{36}$$

5.2 Covariance matrix estimation

We evaluate the covariance matrix for the data vector Π using 1000 EZmocks described in Section 1. Differences between mocks arise because of sample variance – we probe different patches of the Universe, and shot noise – we sample the density field with different galaxies. These are the primary sources of error in clustering measurements.

For each mock, we compute the weighted monopole and quadrupole moments for each set of optimal redshift weights, for $n_b = 10$ k-bins in the range of $k = 0.01$–$0.2\,h\,\mathrm{Mpc}^{-1}$. From these, we derive the covariance matrix as

$$\mathsf{C} = \frac{1}{N_T - 1} \sum_{n=1}^{N_T} \left[P_{n,\ell,w_{\ell,q_t}}(k_i) - \hat{P}_{\ell,w_{\ell,q_t}}(k_i) \right]$$
$$\times \left[P_{n,\ell,w_{\ell,q_t}}(k_j) - \hat{P}_{\ell,w_{\ell,q_t}}(k_j) \right], \tag{37}$$

where $N_T = 1000$ is the number of mock catalogues, w_{ℓ,q_t} denotes each set of weights for each parameter q_t (or p_t) and $\hat{P}_{\ell,w_{\ell,q_t}}(k_i) = \frac{1}{N_T} \sum_{n=1}^{N_T} P_{n,\ell,w_{\ell,q_t}}(k_i)$.

Note that when inverting the covariance matrix we include the Hartlap factor (Hartlap, Simon & Schneider 2007) to account for the fact that C is inferred from mock catalogues. The choice of $n_b = 10$ given $N_T = 1000$ mocks available ensures that the covariance matrix is positive definite.

5.3 Maximizing the likelihood

Since each weighted multipole $P_{i,w_{i,q_j}}$ is optimized with respect to a particular piece of information (e.g. $\Omega_m[z]$), we jointly fit all three q_i (or p_i) parameters simultaneously. We compare the measured Π^T to modelled weighted power spectra multipoles, convolved with the window function as explained in Section 4.2. We assume a Gaussian likelihood and minimize

$$\chi^2 \propto (\Pi - \Pi_{model})^T \mathsf{C}^{-1} (\Pi - \Pi_{model}). \tag{38}$$

Where Π_{model} refers to the window convolved $P_{i,w_{i,q_j}}$. The C^{-1} term corresponds to the joint covariance derived in equation (37). We repeat the fit for both the Ω_m and $f\sigma_8$ optimized sets of weights.

In this analysis we limit ourselves to linear order deviations about our fiducial ΛCDM model, for both $f\sigma_8(z)$ and $\Omega_m(z)$ described in Sections 2.1 and 2.2, since the data cannot capture second-order deviations. We discuss this further in Section 7.

6 MEASURING RSD WITH THE EVOLVING GALAXY POWER SPECTRUM

The fits presented in this section are performed using a Markov chain Monte Carlo (MCMC) code, implemented to efficiently account for the degeneracies between the parameters; in all the fit performed we select a range between $k = 0.01$ and $0.2\,h\,\mathrm{Mpc}^{-1}$. For each scenario explored we run 10 independent chains, satisfying the Gelman–Rubin convergence criteria (Gelman & Rubin 1992) with the requirement of $R - 1 < 10^4$, where R corresponds to the ratio between the variance of chain mean and the mean of chain variances. All the results presented are obtained after marginalizing on the full set of parameters, including the nuisance parameters (shot noise and velocity dispersion). All the contour plots are produced using the public GetDist libraries.[3]

We fit the weighted monopole and quadrupole computed on a subset of 20 EZmocks, for both the Ω_m and the $f\sigma_8$-optimized weights, while keeping the distance–redshift relation fixed to the fiducial cosmology, i.e. $\alpha_\parallel = \alpha_\perp = 1$.
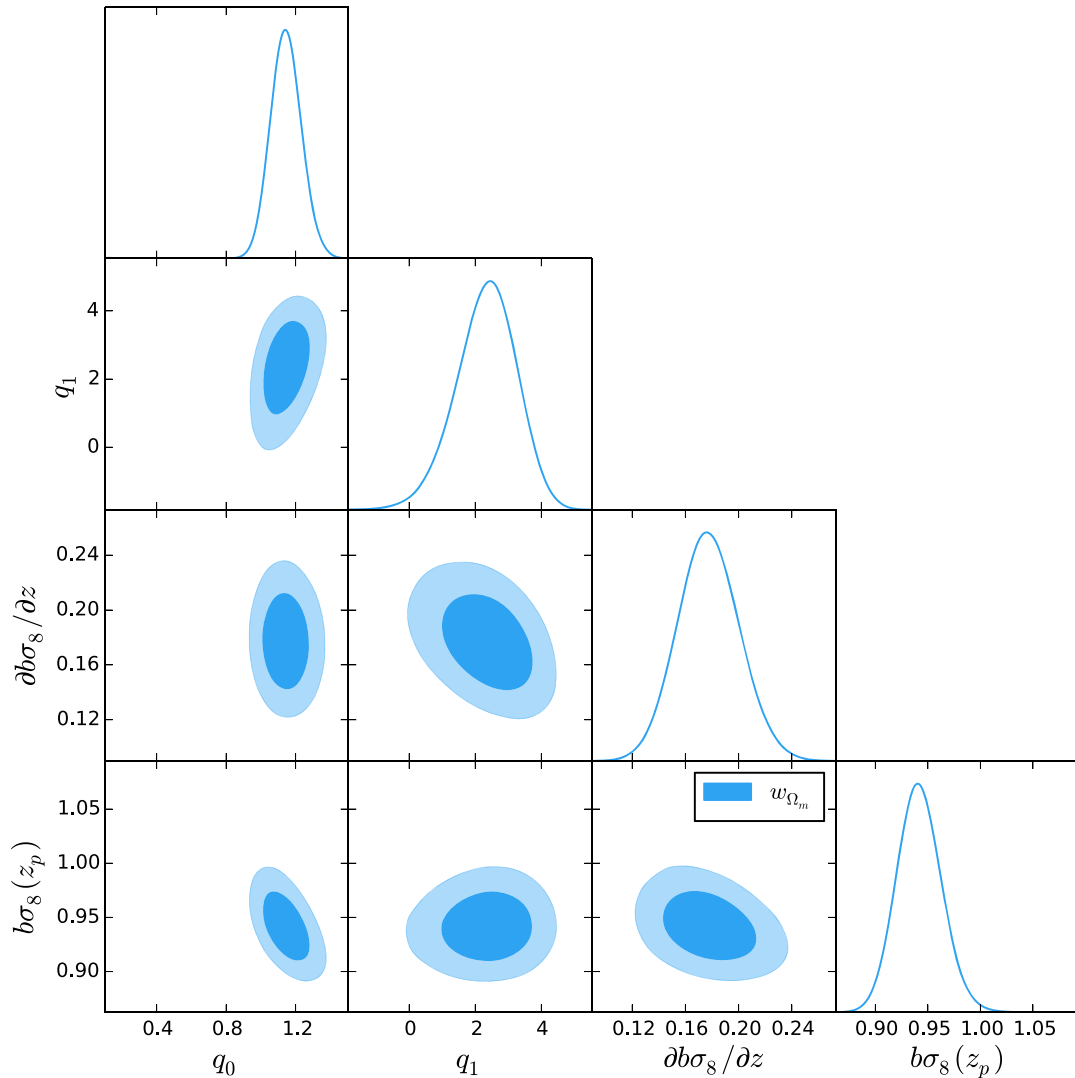
---

[3]http://getdist.readthedocs.io/

Figure 2. Likelihood distributions for the analysis of the average of 20 EZmocks. We show the results for q_0, q_1, $b\sigma_8(z_p)$, $\partial b\sigma_8/\partial z$, marginalized over the full set parameters (including $b_2\sigma_8(z_p)$, σ_v, S not displayed here). We multifit two weighted monopoles and two weighted quadrupoles [one for each weight function (w_{0,p_i}, w_{2,p_i})]. The fitting range is $k = 0.01$–$0.2\,h\,\mathrm{Mpc}^{-1}$ for both the monopole and quadrupole.

We do not consider the full set of 1000 EZmocks for the following reasons: first, we are limited by the EZmocks accuracy in describing non-linearities in galaxy bias and velocities; further by the accuracy in the light-cone describing the redshift evolution for $f\sigma_8$ that is included as a step function. Thus we do not believe that the mocks support us looking at deviations from the model at better accuracy than this. However, the error on our constraints is still $1/\sqrt{20}$ smaller than what we expect on the eBOSS quasars constraints. The analysis has been performed on different subset of 20 mocks out of the 1000 available to verify that the outcomes do not depend on a particular subsample choice.

Our analysis is presented as follow. In Section 6.1, we present the result obtained with the Ω_m weights fitting for q_0, q_1, $b\sigma_8(z_p)$, $\partial b\sigma_8/\partial z|_{z_p}$, b_2, σ_v, and shot noise S. In parallel we present the fit for p_0, p_1, $b\sigma_8(z_p)$, $\partial b\sigma_8/\partial z|_{z_p}$, b_2, and σ_v when applying the $f\sigma_8$ weights.

In Section 6.2, we investigate the impact of the bias assumption on the constraints, showing a comparison between bias evolving and constant with redshift.

In Section 6.3, we compare the results obtained with the redshift weights approach with the analysis performed considering one *constant* redshift slice, i.e. considering all the parameters ($f\sigma_8$, $b\sigma_8$, σ_v, b_2, S) in the power spectra at their value at the pivot redshift $z = 1.55$ and applying FKP weights only (for simplicity of the notation from now on we refer to this as *traditional* analysis).

Differently from Zhu et al. (2016), we compare the redshift weights analysis with the standard analysis used for previous RSD measurements (see e.g. Beutler et al. (2017)) rather than testing the weights $w_{q,i}$, $w_{p,i} = 1$. The main focus of this work is to test that our analysis is not biased by introducing evolution in the power spectrum and in the window function. We rely on the Fisher matrix
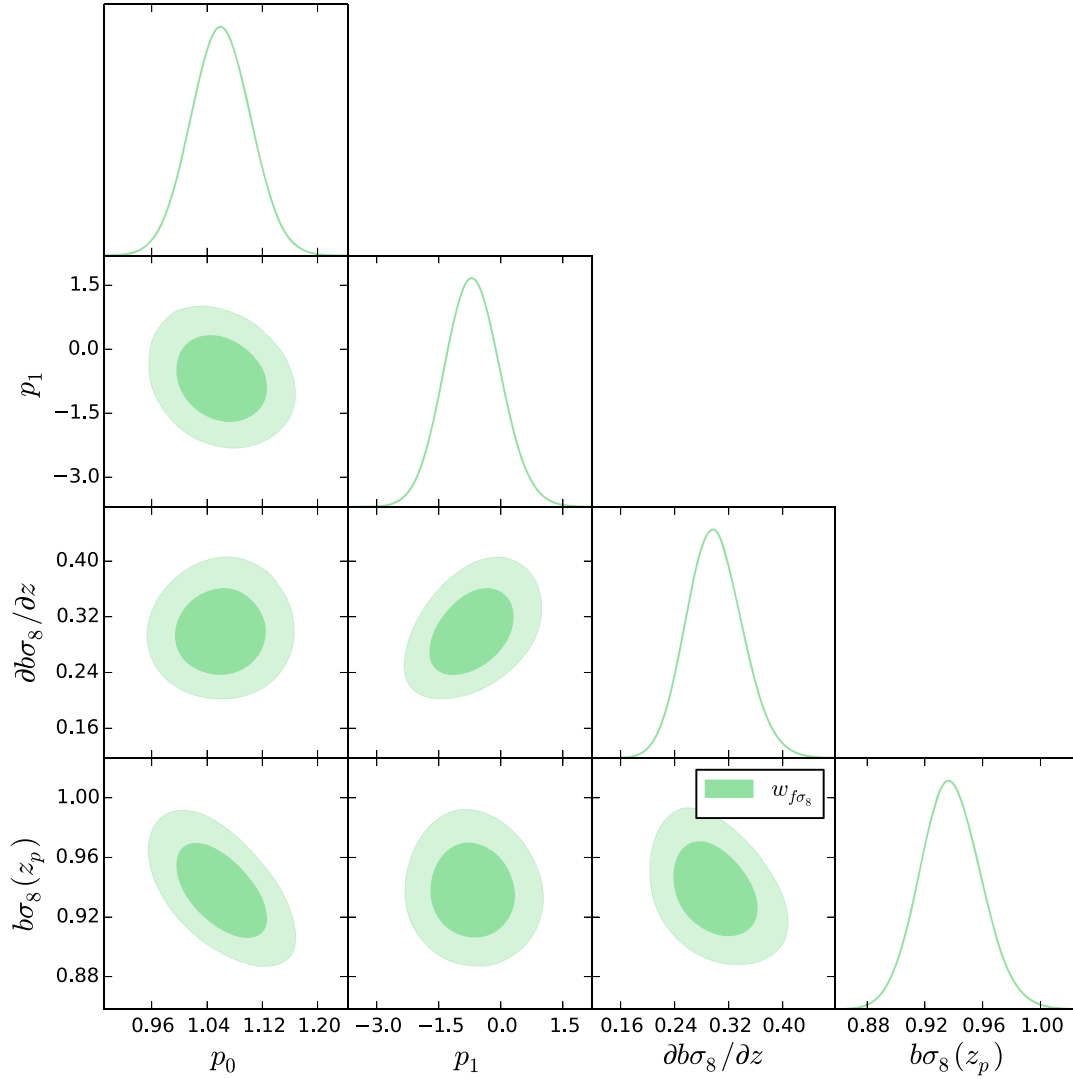
Figure 3. Likelihood distributions for the analysis of the average of 20 EZmocks. We show the results for p_0, p_1, $b\sigma_8(z_p)$, $\partial b\sigma_8/\partial z$, marginalized on the full set parameters (including $b_2\sigma_8(z_p)$, σ_v, S not displayed here). We multifit two weighted monopoles and two weighted quadrupoles [one for each weight function (w_{0,p_i}, w_{2,p_i})]. The fitting range is $k = 0.01$–$0.2\,h\,\mathrm{Mpc}^{-1}$ for both the monopole and quadrupole.

theory correctly selecting the set of weights optimal with respect to the q_i, p_i errors.

6.1 Redshift weights fit

Fig. 2 shows the posterior likelihood distributions from the analysis performed with the set of redshift weights optimized to constrain $\Omega_m(z)$ (blue contour plots), using the monopole and the quadrupole; we fit for q_0, q_1 that describe up to linear order deviations in the evolution of $\Omega_m(z)$ according to ΛCDM model; we also vary the galaxy bias parameters modelled as in Section 4.3, while we fix the second-order non-local bias, bs_2, and third-order non-local bias, $b_{3\mathrm{nl}}$, terms as shown in equation (35). To summarize we fit for seven parameters: q_0, q_1, $b\sigma_8(z_p)$, $\partial b\sigma_8/\partial z|_{z_p}$, $b_2\sigma_8(z_p)$, σ_v, and shot noise S.

Fig. 3 presents the results of the analysis while using the set of redshift weights optimized to constrain $f\sigma_8(z)$, as introduced in Section 2.2; the structure is the same as in Fig. 2. We fit for p_0, p_1

to constrain $f\sigma_8(z)$ deviations about the fiducial $f\sigma_8(z)$ according to ΛCDM; we also fit for $b\sigma_8(z_p)$, $\partial b\sigma_8(z)/\partial z$, $b_2\sigma_8(z_p)$, σ_v, and S, seven parameters in total as for the other set of weights.

We obtained the covariance and correlation matrix for the full set of parameters of the MCMC chains using GetDist libraries. The resulting posteriors in both Figs 2 and 3 show a correlation between the zero-order parameters, q_0 (p_0) and $b\sigma_8(z_{\mathrm{piv}})$, of magnitude of ~ 0.5. We also detect a relevant anticorrelation $\sim - 0.4$ between the slope parameter q_1 (p_1) and the gradient $\partial b\sigma_8(z)/\partial z$. These non-zero correlations lead to a mild dependency between the assumed bias model (linear and non-linear in k and in z) and the slope parameter q_1 (p_1) without however affecting (within $\sim 1\sigma$) the constraints on $f\sigma_8$. In Section 6.2, we illustrate the impact of the bias evolution on the growth rate in more details. Because of the stepwise implementation of the growth rate and bias model in the mocks, the fiducial values of q_0, q_1 (p_0, p_1) are not well defined. Therefore, we do not display an expected value for p_i and q_i as those cannot be inferred from the $f\sigma_8$ evolution included as a non-smooth
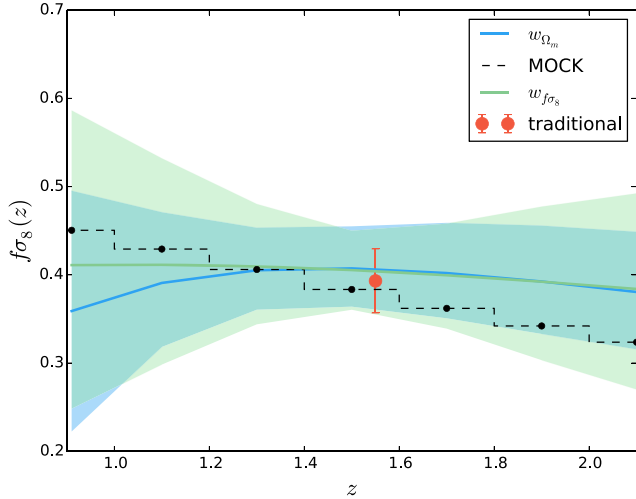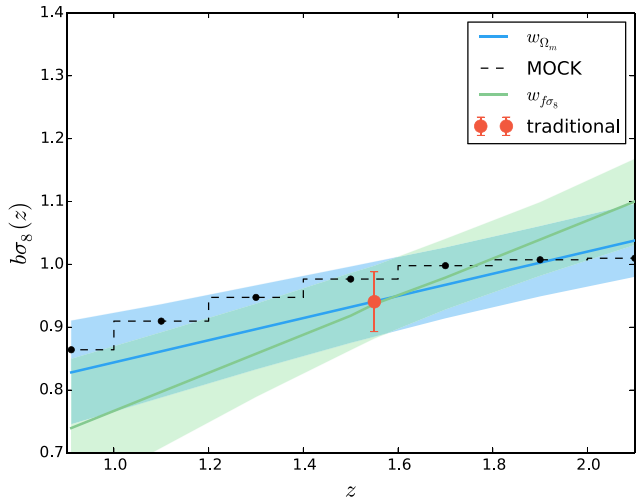
Figure 4. The reconstructed evolution of $f\sigma_8$ and 68 per cent confidence level regions using the average of 20 mocks; blue shaded region shows the constraint on the evolution of $f\sigma_8$ obtained by the fit of $\Omega_{\mathrm{m}}(z, q_i)$ using the $w_{\Omega_{\mathrm{m}}}$ optimal weights and deriving at each redshift $f[\Omega_{\mathrm{m}}(z, q_i)]$ times $\sigma_8[\Omega_{\mathrm{m}}(z, q_i)]$; green shaded region shows the resulting evolution when fitting for $f\sigma_8(z, p_i)$ at each redshift. The red point indicates the results obtained when performing the traditional analysis, with $z_{\mathrm{piv}} = 1.55$.

Figure 5. The reconstructed evolution for $b\sigma_8(z)$ and 68 per cent confidence level regions using the average of 20 mocks; we fit the evolution for $b\sigma_8$, modelled as a Taylor expansion about the pivot redshift, up to linear order. Blue shaded regions show the evolution of $b\sigma_8$ through the fit of $b\sigma_8(z_{\mathrm{p}})$, $\partial b\sigma_8(z)/\partial z$, obtained for the $\Omega_{\mathrm{m}}(q_i)$ analysis; green shaded regions show the analogous resulting $b\sigma_8(z)$ when fitting for $f\sigma_8(z, p_i)$ at each redshift. The red point indicates the results obtained for $f\sigma_8(z_{\mathrm{piv}})$ when performing the traditional analysis.

step function in the mocks. However, within 1σ–2σ we recover the smooth ΛCDM expectation values of $q_0 = 1$ and $q_1 = 0$.

Fig. 4 shows the redshift evolution reconstructed from p_0, p_1 (green shaded regions) compared with the evolution reconstructed from the q_0, q_1 (blue shaded regions). The red point indicates the constraints at one single redshift (traditional analysis, with $z = 1.55$) for $f\sigma_8$. We overplot the evolution of $f\sigma_8(z)$ as accounted in the

mock light-cone (black dashed line). The plot shows that the $f\sigma_8$ evolution obtained for both the Ω_{m} and $f\sigma_8$ weighting schemes is fully consistent with the cosmology contained in the mock and in full agreement with the constraints coming from the traditional analysis. For both parametrizations the errors obtained at the pivot redshift are comparable with the error we get from the traditional analysis. Note that the error from redshift weighting analysis comes from the marginalization over a set of seven parameters in contrast to the traditional analysis limited to only five free parameters.

Away from the pivot redshift, the errors become larger for both parametrizations. At these redshifts, the major contribution to the error comes from the slope constraints (q_1, p_1) and the signal-to-noise ratio (S/N) is lowered due to the low number density $n(z)$ (Ata et al. 2018). The number of quasars observed as a function of redshift also helps to explain the differences in the error as a function of redshift, with a larger error found where there are fewer quasars.

For both parametrizations, the slope parameters are degenerate with the non-linear bias parameters.

In Section 6.1, we modelled the bias evolution with a Taylor expansion up to linear order about the pivot redshift (see equation 4.3). Fig. 5 shows the $b\sigma_8(z)$ evolution measured using the Ω_{m} and $f\sigma_8$ weighting schemes (blue and green shaded regions). We reconstruct $b\sigma_8(z)$ at the different redshifts from the fit of $b\sigma_8(z_{\mathrm{p}})$ and $\partial b\sigma_8(z)/\partial z$. We overplot the evolution of $b\sigma_8(z)$ as included in the mocks (black dashed line). The red point indicates the constraints obtained by using the traditional analysis; we find full agreement at the pivot redshift between the three different analysis and within 1σ of the value included in the mocks. The bias depends significantly on redshift and in the mocks is modelled as a step function, which leads to small discrepancies with respect to both the constant and linear evolution in $b\sigma_8$. We redid the fit extending the analysis to second order in bias and found consistent results but with error too large to see any improvements (high degeneracy). For the purpose of fitting eBOSS quasar sample this is more than enough and we leave for future work a more careful study of the bias effects/evolution to be performed on more accurate N-body mocks. This is discussed further in Section 7.

6.2 Constant bias versus evolving bias

We now investigate how a particular choice for the bias evolution in redshift can affect and impact the constraints on $f\sigma_8(z)$. To do this, we repeat the analysis as presented in Section 6.1 using the Ω_{m} and $f\sigma_8$ weights, we model $\Omega_{\mathrm{m}}(z)$ and $f\sigma_8(z)$ in the same way as in Section 6.1, but now assuming that the bias is constant with redshift, i.e. we set $\partial b\sigma_8(z)/\partial z = 0$.

In Figs 6 and 7, we show the comparison between the results obtained with the constant bias. We display the posterior likelihood for all the quantities evaluated at the pivot redshift, $f\sigma_8(z_{\mathrm{p}})$ $b\sigma_8(z_{\mathrm{p}})$, σ_v, b_2, and S. In Fig. 6, blue contours show the likelihood distributions obtained when using the Ω_{m} weights and considering $b\sigma_8$ evolving as in equation (4.3). Dark blue contours indicate the constraints obtained when considering $\partial b\sigma_8(z)/\partial z = 0$. In Fig. 7, we present the analogous results when using the $f\sigma_8$ parametrization; green contours show the likelihood distributions obtained when using the $f\sigma_8$ weights considering the bias evolving as in equation (4.3). Dark green contours correspond to the constraints obtained when we set $\partial b\sigma_8(z)/\partial z$ equal to zero.

The results obtained from the different models are consistent, but, whereas the constraints for $b\sigma_8(z_{\mathrm{p}})$ remain unchanged, there
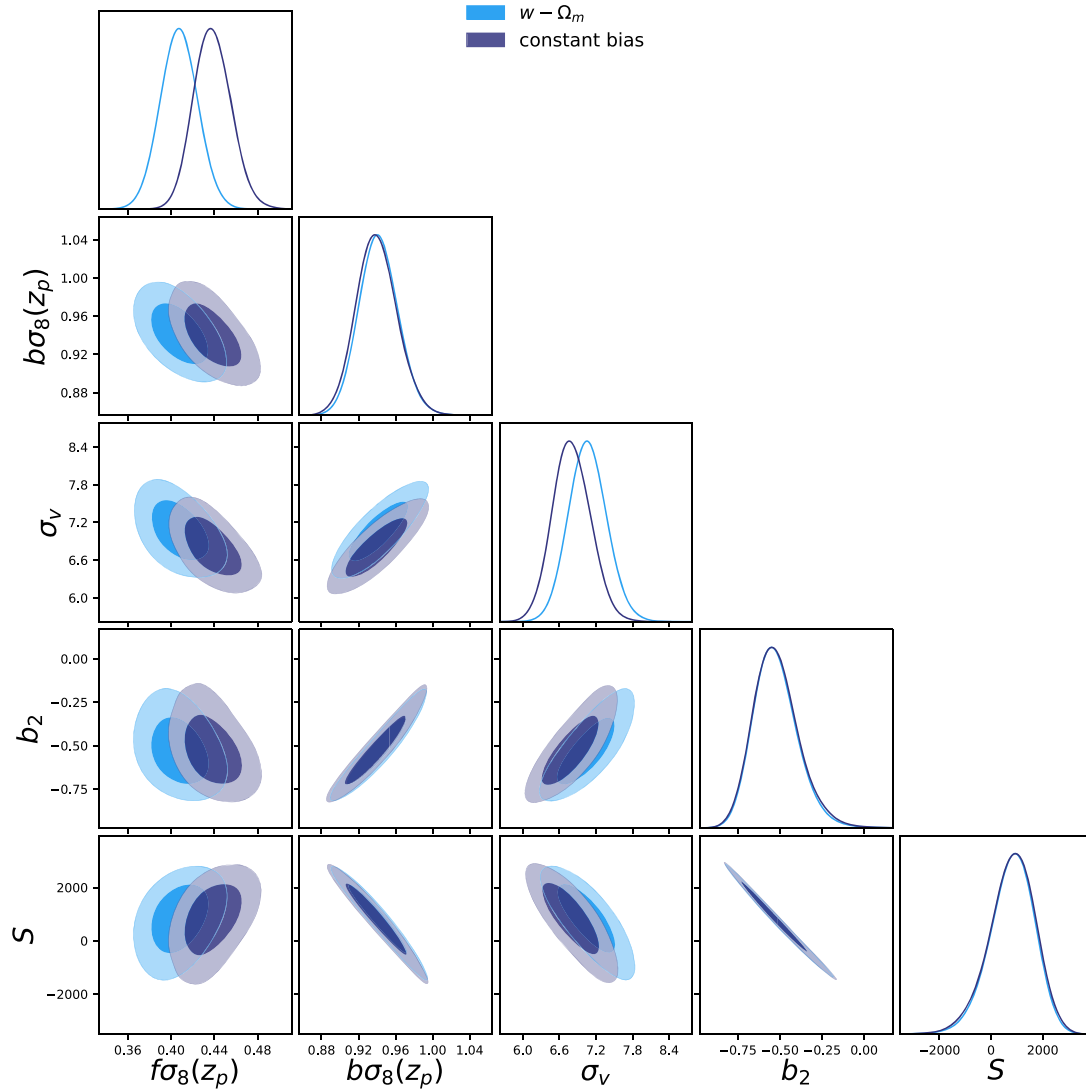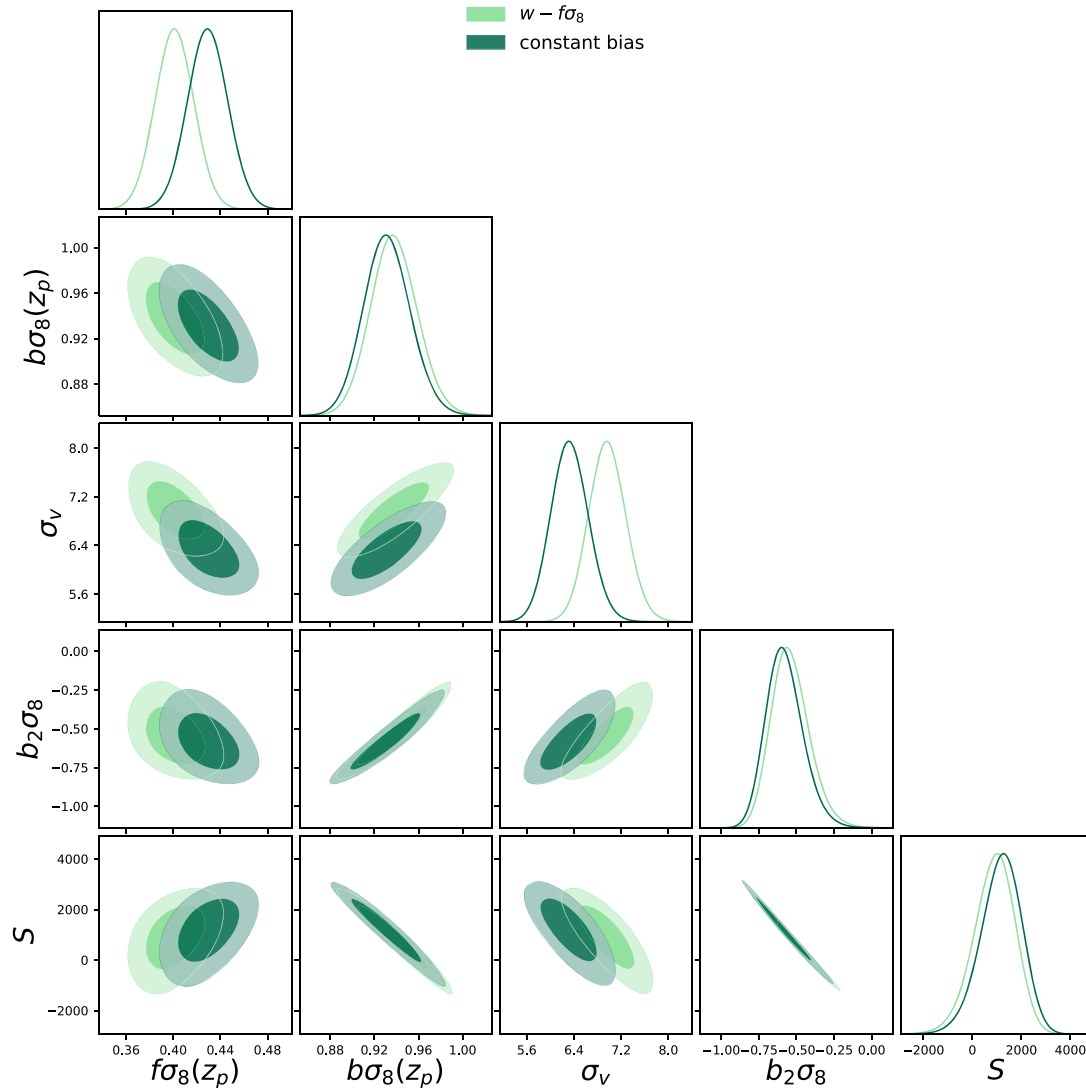
Figure 6. Comparison between evolving and constant bias for the $\Omega_{\rm m}$-weights analysis. Blue likelihood contours indicate the constraints obtained when fitting for $b\sigma_8(z_{\rm p})$ and $\partial b\sigma_8(z)/\partial z$; dark blue contours indicate the constraints obtained when setting $\partial b\sigma_8(z)/\partial z = 0$ and fitting only for $b\sigma_8(z_{\rm p})$.

is an evident impact on the $f\sigma_8$ constraints at the pivot redshift. Forcing the bias to be constant with redshift lead to a higher value for $f\sigma_8$.

This should be more important for future surveys, for which higher precision is expected: for these surveys, a careful study/treatment of the bias will be required. One approach would be to have free functions to describe the bias (e.g. Taylor expanding cosmological quantities as in the present case), and making sure there is enough freedom in the other parameters so that the measurements are applicable to a wide range of cosmological models and targets, with few assumptions. For higher S/N and more realistic mocks it would be interesting to investigate the evolution in redshift of the non-linear bias parameters and the possible impact on $f\sigma_8$. In this work all of the non-linear quantities are considered at a single redshift and our tests are limited to verify that the bias does not affect the measurement of the growth, which is adequate for the current S/N level.

6.3 Weights versus no weights

We compare the analysis performed using the redshift weights approach, as presented in Section 6.1 with the *traditional* analysis at one constant redshift.

The traditional analysis makes use of the power spectrum moments, modelled as in Section 3, to constrain $f\sigma_8$ and $b\sigma_8$ at one single epoch that corresponds to the effective redshift of the survey ($z = 1.55$). We do the comparison for both the $\Omega_{\rm m}$ $f\sigma_8$ weighting schemes.

Fig. 8 shows the comparison between the redshift weights analysis for $\Omega_{\rm m}$ (blue contours), $f\sigma_8$ (green contours), and the constant redshift analysis (brown contours). In order to make the comparison between the three different analysis, we infer from the MCMC chains of q_i and p_i, the $f\sigma_8[z, \Omega_{\rm m}(q_i)]$, and $f\sigma_8(z, p_i)$ valued at the pivot redshifts. We then compare those values with the $f\sigma_8(z_{\rm p})$, $b\sigma_8(z_{\rm p})$ as obtained from the traditional analysis. The last two panels in Fig. 8 show that we recover the same value for

Figure 7. Comparison between evolving and constant bias for the $f\sigma_8$-weights analysis. Green likelihood contours indicate the constraints obtained when fitting for $b\sigma_8(z_p)$ and $\partial b\sigma_8(z)/\partial z$; dark green contours indicate the constraints obtained when setting $\partial b\sigma_8(z)/\partial z = 0$ and fitting only for $b\sigma_8(z_p)$.

b_2 and S where the evolution in redshift is not considered in all the three different analysis; the other constraints on $f\sigma_8$, $b\sigma_8$, and σ_v are fully consistent within $\sim 1\sigma$.

7 CONCLUSION

In this work we present a new approach to measure RSDs when dealing with surveys covering a wide redshift range; the redshift weights, applied to each galaxy within the sample, act as a smooth window on the data, allowing us to compress the information in the redshift direction without loss of information. In this analysis we applied the redshift weighting technique to investigate small deviation from the ΛCDM framework; we selected two different parametrization, allowing for deviation in the matter energy density and the growth rate evolution. We derived multiple sets of weights to optimize each order of those deviations. We extended the window function derivation in order to account for the redshift evolution of the power spectrum.

We compared the results obtained for the different parameters with the traditional analysis, i.e. the analysis performed considering the clustering as constant in the whole volume. We found that the redshift weights technique gives unbiased constraints for the whole redshift range, in full agreement with the traditional analysis performed at the effective redshift.

The constraints obtained fully validate the analysis (Ruggeri et al. 2018) to measure RSD on the eBOSS quasars sample where the error expected on $f\sigma_8$ is about 5 per cent. To apply the same pipeline to future surveys aiming at per cent level accuracy further work will be required; first, we will need to consider quadratic deviations in the evolution for both the q_i and the galaxy bias parameters. In this work we only accounted for those deviations to test the robustness of the fits whereas the signal expected from the quasars sample will not be able to constrain the quadratic evolution.

Another important and interesting aspect would be to account for the AP parameters and their evolution in redshift. To perform such analysis, a set of N-body simulations that accurately describe non-linearities/light-cone evolution is also required, to reduce the
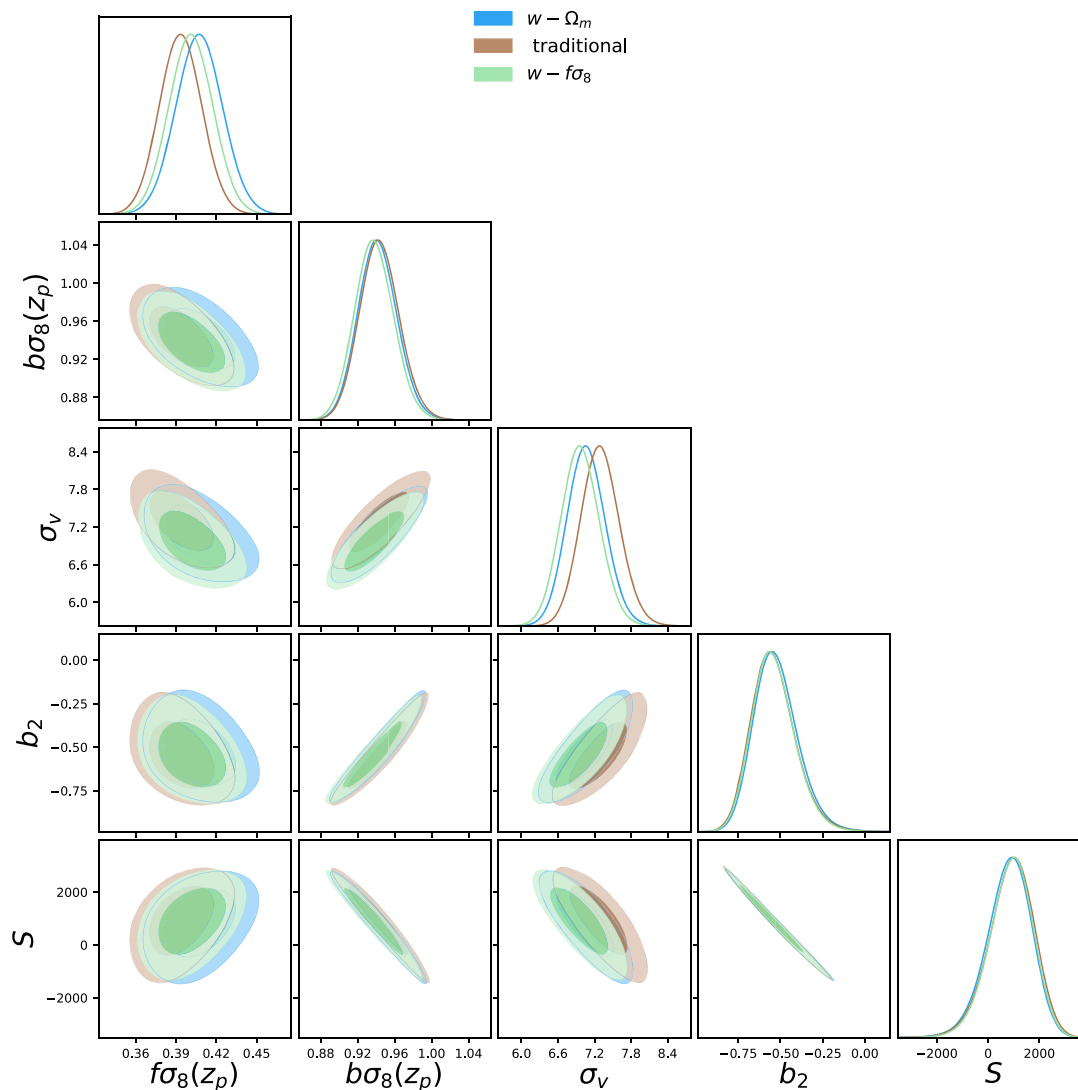
Figure 8. Comparison between the redshift weights analysis and the traditional analysis. Likelihood contours for $f\sigma_8$, $b\sigma_8$, σ_v b_2, and S quantities, at their pivot redshift values. Blue likelihood contours show the results obtained with the $\Omega_m(q_i)$ analysis; green contours show the results from the $f\sigma_8(p_i)$ analysis; brown contours indicate the results obtained with the traditional analysis.

degeneracies and provide a lower statistical error. We here only considered the growth alone, with better data we would be able to include both AP and growth. For the eBOSS sample, the constraints are too weak to consider this.

REFERENCES

Alam S. et al., 2017, MNRAS, 470, 2617
Alcock C., Paczynski B., 1979, Nature, 281, 358
Anderson L. et al., 2014, MNRAS, 441, 24
Ata M. et al., 2018, MNRAS, 473, 4773
Baldauf T., Seljak U., Desjacques V., McDonald P., 2012, Phys. Rev. D, 86, 083540
Beutler F. et al., 2017, MNRAS, 466, 2242
Bianchi D., Gil-Marín H., Ruggeri R., Percival W. J., 2015, MNRAS, 453, L11
Blanton M. R. et al., 2017, AJ, 154, 28
Chan K. C., Scoccimarro R., Sheth R. K., 2012, Phys. Rev. D, 85, 083509
Chuang C.-H., Kitaura F.-S., Prada F., Zhao C., Yepes G., 2015, MNRAS, 446, 2621
Dawson K. S. et al., 2016, AJ, 151, 44
Feldman H. A., Kaiser N., Peacock J. A., 1994, ApJ, 426, 23
Gelman A., Rubin D., 1992, Stat. Sci., 7, 457
Hartlap J., Simon P., Schneider P., 2007, A&A, 464, 399
Kaiser N., 1987, MNRAS, 227, 1
Klypin A., Yepes G., Gottlöber S., Prada F., Heß S., 2016, MNRAS, 457, 4340
Laurent P. et al., 2017, J. Cosmol. Astropart. Phys., 07, 017
Lewis A., Bridle S., 2002, Phys. Rev. D, 66, 103511
Mueller E.-M., Percival W. J., Ruggeri R., 2018, MNRAS, in press (arXiv: 1702.05088)
Planck Collaboration XIII, 2016, A&A, 594, A13
Ruggeri R., Percival W. J., Gil-Marín H., Zhu F., Zhao G.-B., Wang Y., 2017, MNRAS, 464, 2698
Ruggeri R. et al., 2018, preprint (arXiv:1801.02891)
Scoccimarro R., 2004, Phys. Rev. D, 70, 083007
Scoccimarro R., 2015, Phys. Rev. D, 92, 083532
Song Y.-S., Percival W. J., 2009, J. Cosmol. Astropart. Phys., 10, 004
Springel V., 2005, MNRAS, 364, 1105
Taruya A., Nishimichi T., Saito S., 2010, Phys. Rev. D, 82, 063522
Wilson M. J., Peacock J. A., Taylor A. N., de la Torre S., 2017, MNRAS, 464, 3121
Yamamoto K., Nakamichi M., Kamino A., Bassett B. A., Nishioka H., 2006, PASJ, 58, 93
Zhao G.-B. et al., 2016, MNRAS, 457, 2377
Zhu F., Padmanabhan N., White M., 2015, MNRAS, 451, 236
Zhu F., Padmanabhan N., White M., Ross A. J., Zhao G., 2016, MNRAS, 461, 2867

This paper has been typeset from a TEX/LATEX file prepared by the author.